WILEY | Hindawi

Research Article

N-Doped Graphene Nanofibers with Porous Channel Comprising Fe_xS_y Nanocrystals and Intertwined N-Doped CNTs as Efficient Interlayers for Li-S Batteries

Chan Sic Kim ⓘ, Rakesh Saroha ⓘ, and Jung Sang Cho ⓘ

Department of Engineering Chemistry, Chungbuk National University, Chungbuk 361-763, Republic of Korea

Correspondence should be addressed to Jung Sang Cho; jscho@cbnu.ac.kr

Hierarchically porous and conductive nanofibers (NFs) comprising nitrogen-doped reduced graphene oxide (N-rGO) and iron sulfide (Fe_xS_y) nanocrystals along with highly intertwined nitrogen-doped carbon nanotubes (N-CNTs) abbreviated as "P-rGO@Fe_xS_y/N-CNT NFs" were synthesized *via* electrospinning technique as multifunctional interlayers *via* coating on the commercial separator for stable lithium-sulfur (Li-S) batteries. The porous N-rGO framework acts as a backbone to enhance the structural integrity of the nanostructure. The N-CNTs and N-rGO guarantee various conductive channels for quick electron transfer thus allowing fast redox reactions. The thermal breakdown of polystyrene (PS) resulted in the formation of continuous longitudinal channels. Correspondingly, the Li-S cell incorporating the P-rGO@Fe_xS_y/N-CNT NF-modified separator and S electrode ($2.41\,mg\,cm^{-2}$) exhibited boosted electrochemical properties such as justifiable rate capability and steady cycling performance (after 800 charge-discharge, cell exhibits a capacity of $464\,mAh\,g^{-1}$ with 44% retention at 0.1 C). The novel synthesis strategy discussed herein will provide significant intuitions to the advancement of innovative nanostructures for different rechargeable purposes.

1. Introduction

Lithium-sulfur (Li-S) batteries are recognized as a favourable alternative for presently commercialized lithium-ion batteries (LIBs) due to high value of theoretical capacity ($1675\,mAh\,g^{-1}$), high average operating voltage (~2.1 V relative to Li^+/Li), low toxicity, and surplus raw material, i.e., elemental sulfur [1–3]. However, its practical feasibility is hindered due to the high insulating nature of sulfur, parasitic "shuttle effect," and large volume variations during lithiation/delithiation resulting in low-rate capability, poor cycling stabilities, high-capacity fading, and low Coulombic efficiencies [4, 5]. Numerous approaches have been adopted to overwhelm these drawbacks, including carbon/S composites [6], chemical and physical confinement of polysulfide species using various polar materials such as metal oxides [7], metal selenides [8], and metal nitrides [9], and electrolyte modulation [10]. Recently, introducing porous nanostructures comprising polar materials along with a highly conductive framework as functional interlayers is considered another effective strategy to restrict polysulfide diffusion and enhance the overall performance [11]. The porosity of the nanostructure is promising for effective electrolyte percolation and smooth diffusion of charged species whereas a conductive framework guarantees the rapid diffusion of charged particles *via* numerous conductive pathways [10]. Likewise, the availability of polar materials ensures enormous chemisorption sites for effective confinement and electrocatalytic reduction of polysulfide species. Transition metal sulfides, denoted as M_xS_y where M represents transition metals such as Fe, Co, and Ni, have been the subject of

extensive research due to their remarkable ability to anchor polysulfides [12]. Besides, the nearly metallic nature of transition metal sulfides offers fast electron transfer over conventional metal oxides such as thus permitting kinetically facilitated electrocatalytic transition of polysulfides species [13].

Herein, we synthesized hierarchically porous and highly conductive one-dimensional (1D) nanofibers (NFs) consisting of nitrogen-doped reduced graphene oxide (N-rGO) and iron sulfide (Fe_xS_y) nanocrystals along with highly intertwined nitrogen-doped carbon nanotubes (N-CNTs) abbreviated as "P-rGO@Fe_xS_y/N-CNT NFs" *via* conventional electrospinning technique followed by heat treatments. The prepared nanostructure was thus utilized as a functional interlayer *via* coating onto a commercial separator for highly stable LSBs. The porosity of the nanostructure was introduced through the thermal decomposition of polystyrene (PS), which resulted in continuous longitudinal channels. The porous N-rGO framework acted as a backbone to enhance the structural veracity of the nanostructure besides increasing the overall electrical conductivity. The N-CNTs and N-rGO guarantee various conductive channels for fast electron transfer thus allowing fast redox reactions. Moreover, the Fe_xS_y nanocrystals offer efficient confinement and electrocatalytic transition of the polysulfide groups. Owing to their structural merits, the P-rGO@Fe_xS_y/N-CNT NFs, as functional interlayers, exhibited good rate capability and extended cycling stability.

2. Materials and Methods

2.1. Sample Preparation.
The hierarchically porous N-doped reduced graphene oxide nanofibers comprising Fe_xS_y nanocrystals and highly intertwined N-CNTs were prepared by conventional electrospinning process followed by posttreatment processes. For spinning solution, 0.1 g of multiwalled carbon nanotubes (MWCNTs) sourced from Cheap Tubes Inc., Cambridgeport, USA (with an outer diameter of 20–30 nm, length of 10–30 mm, and purity exceeding 95.0 wt%) along with 0.1 g of graphene oxide (GO) nanosheets was dispersed in 20 mL of dimethylformamide (DMF) from Samchun (99.5% purity). Afterward, 1.0 g of iron(III) acetylacetonate (Fe(acac)$_3$) by Junsei (99.0% purity), 1.0 g of polyacrylonitrile (PAN, Mw: 150,000, Sigma-Aldrich), and 1.5 g of polystyrene (PS, Mw: 192,000, Sigma-Aldrich) were added to the above suspension with continuous stirring overnight. The CNTs were purified *via* acid treatment using a HNO$_3$/H$_2$SO$_4$ (1:3 vol%) solution and washed with deionized water and ethyl alcohol repeatedly. Consequently, the acid-modified CNTs were freeze-dried. GO was prepared *via* the modified Hummers method using graphite flakes. The prepared colloidal solution was filled into a syringe pump (12 mL) equipped with a stainless-steel needle (21-gauge). The solution was then dispensed at a rate of 1.0 mL h^{-1}. The drum collector was rotated at 180 rpm, maintaining a fixed distance of 15 cm between the Al foil collector and the needle tip. An applied voltage of 20 kV was used between the collector and syringe tip. The as-spun composite fibers underwent a stabilization process at 100°C for 2 h in an air atmosphere. Subsequently, they were treated at 310°C for 30 min with a heating rate of

5°C min^{-1} in an air atmosphere. Finally, sulfidation was conducted at 300°C for 3 h under H$_2$S atmosphere in the presence of thiourea. As a result, the hierarchically porous N-doped reduced graphene oxide nanofibers comprising biphasic iron sulfide nanocrystals and highly intertwined N-CNTs were obtained and abbreviated as "P-rGO@Fe_xS_y/N-CNT" NFs. For comparison, PAN-derived dense or filled carbon nanofibers (F-CNF) were also synthesized using the identical process. The as-spun PAN-derived fibers were initially stabilized overnight at 150°C and then for 1 h at 200°C in an air atmosphere. The stabilized fibers were then carbonized by heat treatment at 400°C for 3 h under N$_2$ atmosphere.

2.2. Characterization Techniques.
The microstructural analysis of the synthesized nanofibers was observed using field-emission scanning electron microscopy (FE-SEM) using an Ultra Plus instrument from Zeiss. Additionally, field-emission transmission electron microscopy (FE-TEM) was employed for a more detailed analysis using a JEM-2100F microscope from JEOL, which is available at the Korea Basic Science Institute (Daegu). The crystal structures and phases determination were performed using X-ray diffraction (XRD, Bruker, D8 Discover) using Cu K$_{\alpha 1}$ radiation (1.5405 Å), at the Korea Basic Science Institute (Daegu). The crystalline structure of the carbonaceous materials was characterized using Raman spectroscopy (LabRam, HR800, Horiba Jobin-Yvon). The chemical bonding of various elements was analyzed by X-ray photoelectron spectroscopy (XPS, K-Alpha, Thermo Scientific).

2.3. Electrochemical Measurements.
The P-rGO@Fe_xS_y/N-CNT NF-modified separator was prepared using a slurry casting method. Briefly, P-rGO@Fe_xS_y/N-CNT NFs, carbon black (Super P), and polyvinylidene difluoride (PVDF) binder were mixed in 7:2:1 weight ratio and disseminated in *N*-methyl-2-pyrrolidone (NMP) and stirred overnight to obtain homogeneous mixture. The mixture was spread onto commercial Celgard 2400 polypropylene separator *via* doctor blade process. The coated separator was placed at 60°C overnight and subsequently pressed into round disks ($\phi = 19$ mm and loading = 0.5 mg cm^{-2}). The sulfur cathodes were obtained by dispersing elemental S, carbon black, and PVDF in NMP 7:2:1 weight ratio, respectively. The slurry was casted onto an Al foil, which was continuously dried at 60°C overnight to remove the solvent. Afterward, round electrodes ($\phi = 14$ mm) with an average sulfur loading of 2.41 mg cm^{-2} were subsequently pressed. Li metal as the counter electrode and Celgard 2400 polypropylene film as separator were used. A 1.0 mol L^{-1} lithium bis(trifluoromethanesulfonyl)imide (LiTFSI) was used as the electrolyte. The solution was prepared by dissolving LiTFSI in a mixture of 1,3-dioxolane (DOL) and 1,2-dimethoxyethane (DME) in a 1:1 volume ratio. Additionally, 0.5 mol L^{-1} of lithium nitrate (LiNO$_3$) was included as an additive to the electrolyte solution. 2032-type coin cells were assembled inside an Ar-filled glove box. The volume of electrolyte was limited to 20 μL mg^{-1} inside the cells. Cyclic voltammetry (CV) measurements were performed at a scan rate of 1.0 mV s^{-1}. The galvanostatic characteristics were investigated by cycling in a potential window of 1.7–2.8 V at various C rates. The C
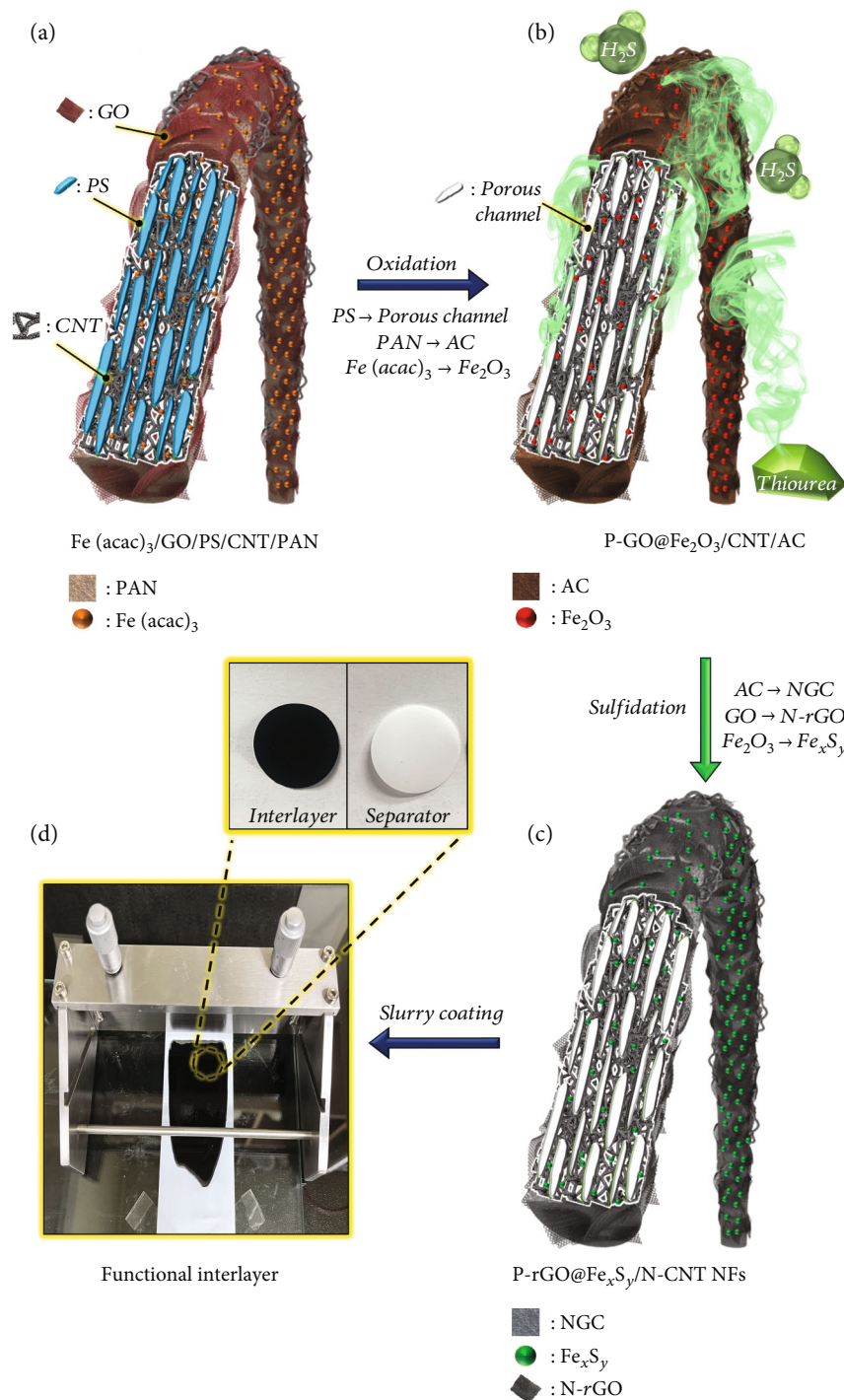
SCHEME 1: Schematic illustration of detailed formation mechanisms (a, b, and c) for hierarchically porous and highly conductive nanofibers consisting of N-doped rGO and Fe_xS_y nanocrystals along with highly intertwined N-doped CNTs (P-rGO@Fe_xS_y/N-CNT NFs) and (d) its digital photographs after slurry coating as a functional interlayer.

rate was determined by equating 1.0 C to $1675\,mA\,h\,g^{-1}$. The cycling property was also examined at 0.1 C rate.

3. Results and Discussion

The detailed experimental procedure to obtain P-rGO@Fe_xS_y/N-CNT NFs along with the complete physical and electro-chemical characterization techniques is provided in the Supporting Information. Scheme 1 shows the detailed formation mechanism of P-rGO@Fe_xS_y/N-CNT NFs. The as-spun Fe(acac)$_3$/GO/PS/CNT/PAN composite fibers (Scheme 1(a)) comprised a homogeneously distributed metal precursor, GO flakes, elongated PS, and N-CNTs well grafted inside the PAN matrix. The elongation of PS under an electric field is
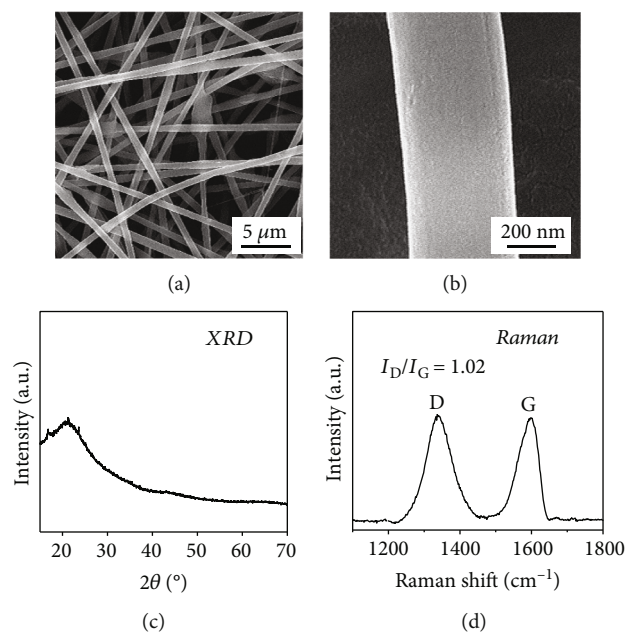
FIGURE 1: Characterization of as-spun Fe(acac)$_3$/GO/PS/CNT/PAN composite fibers stabilized at 100°C: (a, b) FE-SEM micrographs, (c) XRD pattern, and (d) Raman spectrum.

mainly due to the different solubility extents of PAN and PS phases in the DMF solvent [11]. The oxidation process of the as-spun stabilized fibers (Scheme 1(b)) resulted in the thermal breakdown of the elongated PS, thus forming continuous tunnel-like longitudinal channels. In addition, the PAN matrix was transferred to the amorphous carbon (AC) framework, whereas the Fe precursor was converted to the Fe$_2$O$_3$ phase. The sulfidation process using thiourea (Scheme 1(c)) implies that the AC was converted to nitrogen-doped graphitic carbon (NGC) owing to the catalytic nature of the Fe species, whereas the GO was transformed to nitrogen-doped reduced GO (N-rGO). Similarly, the Fe$_2$O$_3$ nanocrystals were converted to iron sulfide (Fe$_x$S$_y$) nanoparticles embedded inside the N-rGO framework. Additionally, the highly intertwined N-CNTs were believed to remain intact and well grafted inside the carbon skeleton throughout the synthesis process. The as-prepared P-rGO@Fe$_x$S$_y$/N-CNT NFs were then applied as multifunctional interlayers *via* a slurry-coating process (Scheme 1(d)).

The formation mechanism presented in Scheme 1 was further verified by examining the structural and phase changes of the nanofibers after each processing step. The FE-SEM micrographs of the as-spun Fe(acac)$_3$/GO/PS/CNT/PAN composite fibers attained after stabilization at 100°C for 2 h in Figures 1(a) and 1(b) suggest a 1D fibrous morphology for the prepared samples with an average diameter of *ca.* 500 nm. In addition, the smooth fiber surface in Figure 1(b) implies the uniform dispersion of different components inside the fibrous structure. The XRD pattern in Figure 1(c) indicates the amorphous nature of the composite fibers. Furthermore, typical D- and G-band signatures in the Raman spectra (Figure 1(d)) indicated the existence of a carbon framework in the fibers [14]. Besides, a high relative intensity (i.e., I_D/I_G) ratio of *ca.* 1.02 implies the amor-

phous nature of the carbon products, thus confirming the XRD results.

The stabilized fibers were oxidized further at 310°C for 30 min, and the obtained fibers are presented in Figures S1(a)–S1(c). The FE-SEM images of the oxidized fibers, i.e., P-GO@Fe$_2$O$_3$/CNT/AC fibers in Figure S1(a), indicate that the 1D fibrous morphology is intact. In addition, the high-magnification FE-SEM image in Figure S1(b) reveals the formation of continuous longitudinal channels in the fibrous morphology, primarily due to the thermal decomposition of the stretched PS dispersed phase. In addition, the carbonization of the PAN matrix and decomposition of Fe(acac)$_3$ yielded amorphous carbon and Fe$_2$O$_3$ phases, respectively. The XRD pattern (Figure S1(c)) also suggested the formation of a nanocrystalline Fe$_2$O$_3$ phase. Finally, P-rGO@Fe$_x$S$_y$/N-CNT NFs were obtained from the oxidized P-GO@Fe$_2$O$_3$/CNT/AC fibers *via* a sulfidation process at 300°C in a reductive atmosphere (Figure 2). The FE-SEM image in Figure 2(a) again confirms that the fibrous morphology remains unchanged, whereas the high-magnification image in Figure 2(b) indicates the presence of tunnel-like channels along with well-grafted N-CNTs inside the structure. The TEM image in Figure 2(c) firmly validates the fibrous morphology (mean diameter of *ca.* 450 nm) and is consistent with FE-SEM results. Besides, the Fe$_x$S$_y$ nanocrystals are easily observed. The high-resolution TEM (HR-TEM) image in Figure 2(d) reveals the presence of an NGC layer formed owing to the catalytic nature of Fe species along with clear lattice fringe separations of 0.270 and 0.207 nm for the (200) and (206) crystal planes of the FeS$_2$ and Fe$_7$S$_8$ phases, respectively. The selected area electron diffraction (SAED) pattern and the XRD results shown in Figures 2(e) and 2(f), respectively, confirm the existence of the NGC and Fe$_x$S$_y$ phases. The
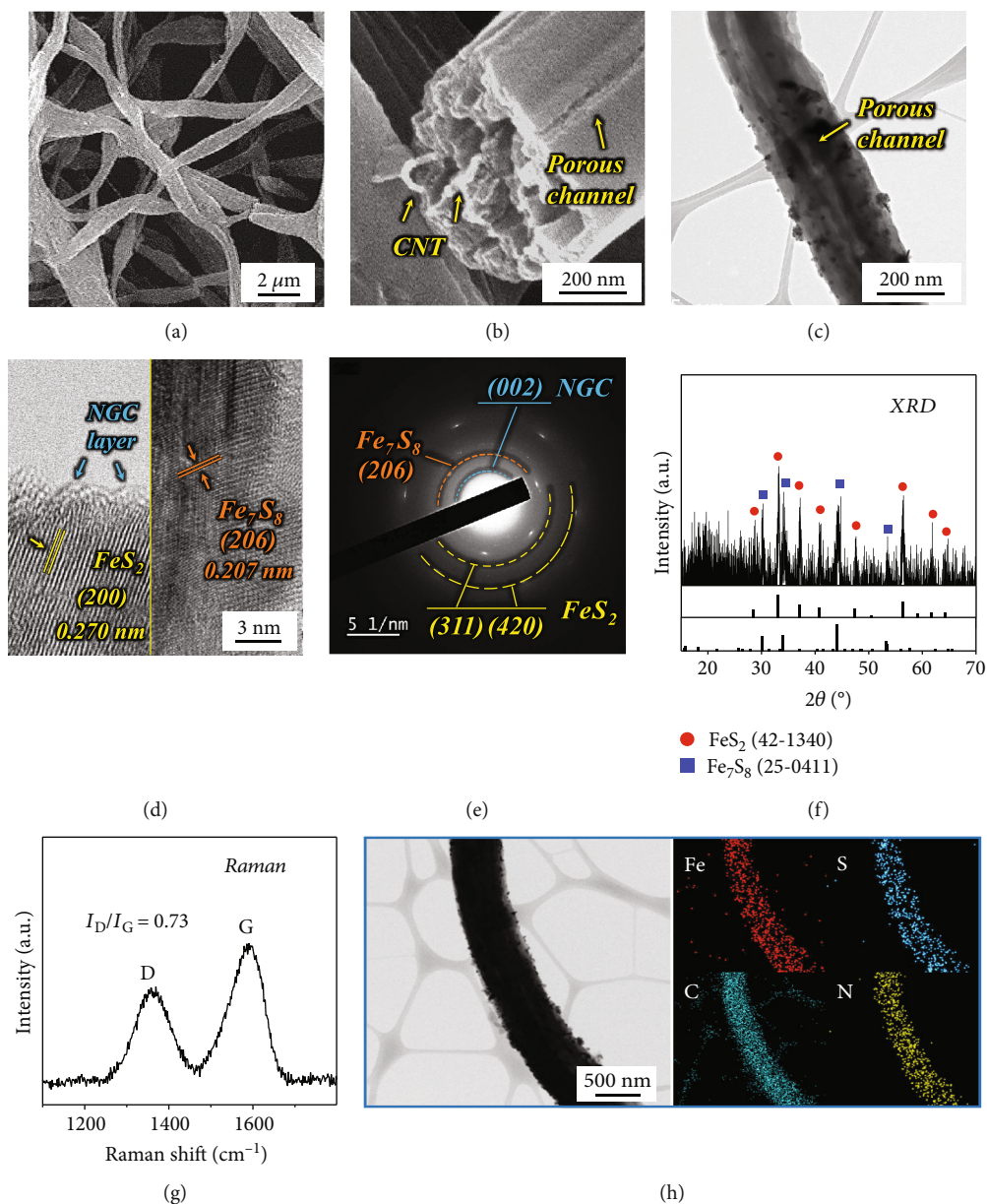
FIGURE 2: Physical characterization results of P-rGO@Fe$_x$S$_y$/N-CNT nanofibers: (a, b) FE-SEM images, (c) TEM image, (d) HR-TEM image, (e) SAED pattern, (f) XRD pattern, (g) Raman spectrum, and (h) elemental dot mapping images.

Raman spectrum in Figure 2(g) indicates that the carbonaceous species in the nanofibers were mainly graphitic, as indicated by the I_D/I_G value of 0.73. The elemental dot mapping images in Figure 2(h) confirm the homogeneous distribution of Fe, S, C, and N throughout the fiber length, thus indicating the presence of an N-doped carbonaceous structure comprising Fe$_x$S$_y$ nanocrystals and well-grafted N-CNTs. For comparison, the FE-SEM images of PAN-derived dense or filled carbon nanofibers (i.e., without GO, N-CNTs, PS, and Fe-salt precursor), abbreviated as "F-CNF," were also obtained, as shown in Figures S2(a) and S2(b), indicating a highly filled structure with a mean diameter of *ca.* 150 nm. Besides, the XRD patterns shown in Figure S2(c) also indicate the

formation of PAN-derived amorphous carbon, with a wide peak at $2\theta = 24°$ corresponding to the (002) plane.

The X-ray photoelectron spectroscopy (XPS) survey spectrum of P-rGO@Fe$_x$S$_y$/N-CNT nanofibers (Figure S3) revealed well-resolved peaks corresponding to the Fe, S, C, and N signals. The Fe 2p spectra in Figure 3(a) exhibit well-fitted peak pairs at 706.4/719.0 eV and 709.7/723.5 eV that correspond to the Fe^{2+} and Fe^{3+} electronic states, respectively [15]. The existence of Fe^{3+} state is due to the surface oxidation of the Fe$_x$S$_y$ nanocrystals, well supported by the appearance of the O 1s peak in the XPS spectrum [16]. The S 2p spectrum in Figure 3(b) includes peaks corresponding to S^{2-}, S$_2^{2-}$, and S-O at 161.78/162.68 eV, 162.98/163.98 eV, and
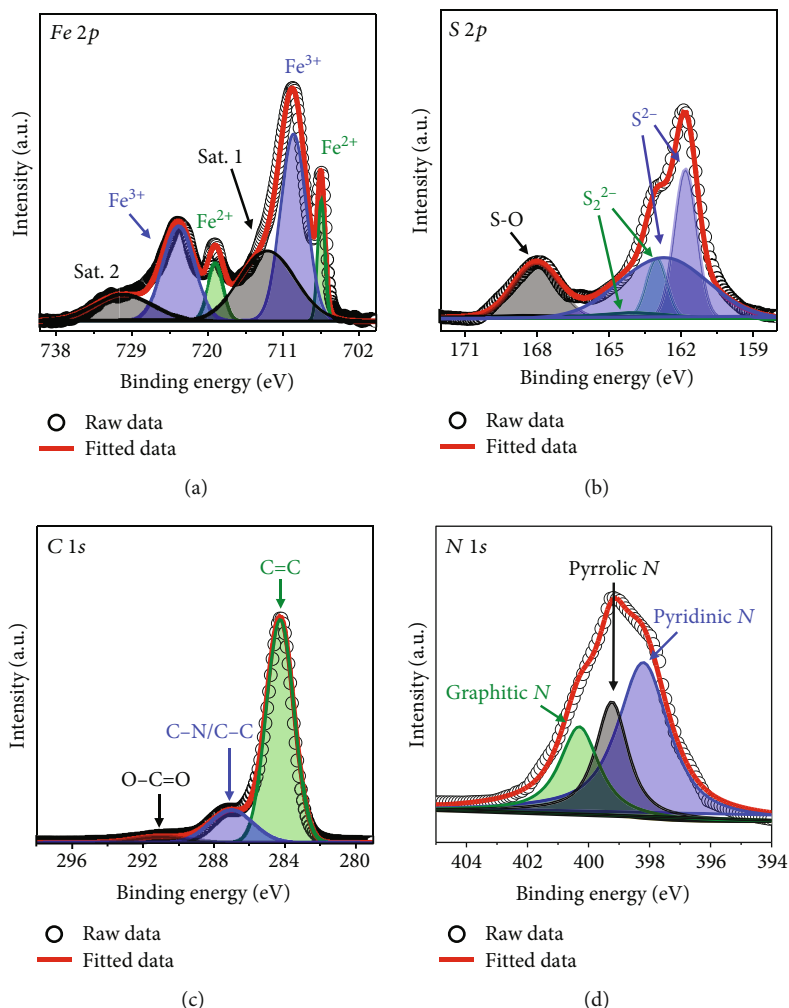
FIGURE 3: XPS spectra of the P-rGO@Fe$_x$S$_y$/N-CNT nanofibers: (a) XPS Fe 2p spectrum, (b) XPS S 2p spectrum, (c) XPS C 1s spectrum, and (d) XPS N 1s spectrum.

168.02 eV, respectively [17]. The S-O bond confirmed the surface oxidation of the nanofibers. The C 1s XPS spectrum in Figure 3(c) displays three peaks at binding energies of 284.2, 287.0 eV, and 290.9 eV, assigned to C=C, C-N/C-C, and O-C=O, respectively [14]. The high intensity of the C=C peak confirms the presence of carbon architecture in the prepared nanofibers [18]. The N 1s deconvoluted spectrum in Figure 3(d) exhibits three peaks corresponding to pyridinic N (398.2 eV), pyrrolic N (399.3 eV), and graphitic N (400.3 eV) species, firmly validating N doping in the nanostructure [19, 20]. The N-doping in the nanostructure enhances the overall conductivity primarily due to the higher electronegativity of the N atom than that of the C atom.

The cyclic voltammetry graphs of Li-S cell pairing elemental S electrode and P-rGO@Fe$_x$S$_y$/N-CNT NF-modified separator in Figure 4(a) exhibit well-separated reduction peaks at 2.26 and 1.91 V, corresponding to the reduction of S to Li$_2$S *via* high- and middle-order polysulfides. The oxidation peak at 2.52 V represents the reverse process, i.e., oxidation of the Li$_2$S back to S *via* middle- and high-order polysulfides. The overlapping CV profiles indicated highly reversible

electrochemical processes. In contrast, the CV profile of the Li-S cell with the F-CNF-modified separator (Figure S4) exhibited comparatively broad and low-intensity redox peaks, suggesting poor redox processes inside the cell. The initial charge-discharge voltage profile in Figure 4(b) also validates the CV results, with the Li-S cell pairing the P-rGO@Fe$_x$S$_y$/N-CNT NF-modified separator exhibiting a high capacity of 1054 mA h g^{-1} compared to 267 mA h g^{-1} for the Li-S cell employing the F-CNF-modified separator at 0.1 C rate. Additionally, the usual charge-discharge voltage plateaus for the P-rGO@Fe$_x$S$_y$/N-CNT NF-modified separator were well synchronized with the CV results, indicating enhanced redox kinetics.

The cycling ability at 0.1 C rate for the cell utilizing the P-rGO@Fe$_x$S$_y$/N-CNT NF-modified separator in Figure 4(c) indicates highly stable prolonged cycling compared to the F-CNF-modified separator. For instance, an initial capacity of 1054 mA h g^{-1} (~63% of the theoretical discharge capacity) was obtained for the P-rGO@Fe$_x$S$_y$/N-CNT NF-modified separator, which stabilized to 464 mA h g^{-1} (44% capacity retention) after 800 continuous charge-discharge cycles, with
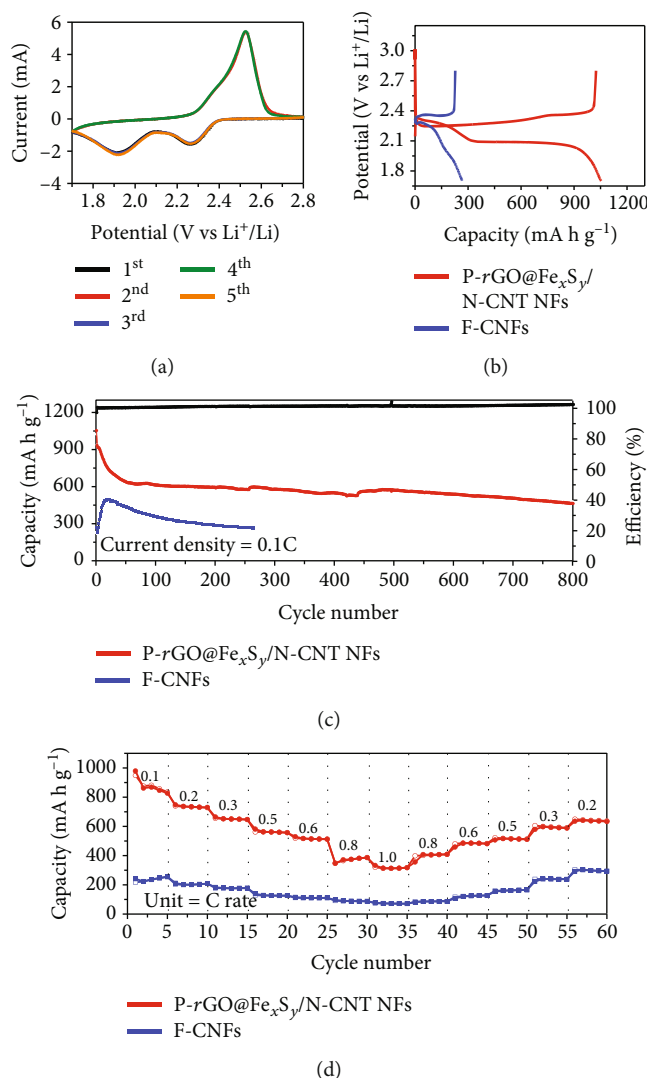
Figure 4: Electrochemical properties of the P-rGO@Fe$_x$S$_y$/N-CNT NFs and F-CNFs: (a) CV curves at 0.1 mV s^{-1} for initial five cycles for the P-rGO@Fe$_x$S$_y$/N-CNT nanofibers, (b) initial charge-discharge profiles at 0.1 C rate, (c) cycle performance at 0.1 C rate, and (d) rate capability test at various C rates.

an average decay rate of just 0.06% per cycle. The stable cycling performance is attributed to the porous and conductive 1D nanostructure, guaranteeing smooth diffusion of charged species and effective volume accommodation besides supporting fast redox reactions *via* instant electron transfer. Additionally, the presence of numerous Fe$_x$S$_y$ chemisorption active sites results in the confinement and reduction of the polysulfide species. In contrast, the F-CNF-modified separator displayed inferior cycling performance, with low discharge values and fast capacity fading characteristics, primarily due to the nonporous nature of the CNFs along with the absence of polar sites, subsequently resulting in a high amount of unused active material and, hence, substandard electrochemical performance.

The rate performances of the Li-S cells featuring different coated separators are presented in Figure 4(d). Li-S cells utilizing the P-rGO@Fe$_x$S$_y$/N-CNT NF-modified separator display an initial discharge capacities of 979, 748, 665, 582,

530, 347, and 333 mA h g^{-1} at a current of 0.1, 0.2, 0.3, 0.5, 0.6, 0.8, and 1.0 C, respectively. Moreover, when the current direction was overturned, the Li-S cell recovered the discharge capacity values significantly. For instance, at a reverse current of 0.2 C, the cell recovered almost 87% of the discharge capacity value. The reasonable rate capability is attributed to the effective confining of polysulfide species by the Fe$_x$S$_y$ nanocrystals, which resulted in high S utilization even at a high C rate of 1.0 C (20% S utilization; Figure S5). In contrast, the Li-S cell utilizing the F-CNF-modified separator exhibited low discharge capacity values at identical C rates, implying poor reaction kinetics. Table 1 compares the obtained performance in this work with previously reported results. Overall, the cycling performance and rate capability tests validate that the structural benefits of the P-rGO@Fe$_x$S$_y$/N-CNT NF have synergetic effects on enhancing the electrochemical functioning of the Li-S cell.

TABLE 1: Comparison of the electrochemical performance of Li-S cell featuring P-rGO@Fe$_x$S$_y$/N-CNT interlayer with the previously reported interlayer materials.

Interlayer materials	Voltage range (V)	S-loading (mg cm^{-2})	Initial C$_{discharge}$ and current rate [mA h g^{-1}]/(C)	Discharge capacity [mA h g^{-1}] and cycle number	Ref.
P-rGO@Fe$_x$S$_y$/N-CNT	**1.7-2.8**	**2.41**	**1054/0.1**	**464/800**	**This work**
Active carbon/RGO	1.0-3.0	—	1078/0.1	655/100	[21]
Acid-treated MWCNTs	1.5-3.0	1.3	1129/0.2	384/200	[22]
SWCNT-PAA	1.5-3.0	2.7	770/1.0	573/200	[23]
Vapor growth CNFs-PPy	1.5-3.0	—	1085/0.1	768/200	[24]
BN/g-C$_3$N$_4$/graphene	1.7-2.7	1.5	1211/0.2	603/500	[25]
Graphite-modified	1.6-2.8	2.0	1029/0.05	698/100	[26]
Vapor growth CNFs-PPy	1.5-3.0	—	1085	768/200	[27]
Co$_9$S$_8$@S nanotube	1.5-3.0	—	900	650/100	[28]

4. Conclusions

In short, we prepared a hierarchically porous 1D nanostructure comprising a nitrogen-doped reduced graphene oxide (N-rGO) matrix as a self-supporting skeleton, well-embedded Fe$_x$S$_y$ nanocrystals, and highly intertwined nitrogen-doped carbon nanotubes (N-CNTs). The P-rGO@Fe$_x$S$_y$/N-CNT synthesized nanostructure was successfully utilized as a multifunctional interlayer to suppress polysulfide crossover inside the Li-S cell. The nanostructure enhances structural integrity and overall electrical conductivity and guarantees abundant conductive channels for fast electron transfer, thus allowing fast redox reactions. These properties resulted in enhanced electrochemical performance, such as satisfactory rate capability and steady cycling performance. Therefore, we expect this design strategy will considerably improve the expertise of developing advanced nanostructures for rechargeable applications.

Data Availability

The data used to support the findings of this study are included within the article.

Conflicts of Interest

The authors declare that there are no competing financial interests.

Authors' Contributions

Chan Sic Kim designed the idea and performed the experiments. Rakesh Saroha performed the experiments and prepared the initial blueprint. Jung Sang Cho gave supervision and writing for the review and editing. Chan Sic Kim and Rakesh Saroha contributed equally to this work.

Acknowledgments

Supplementary Materials

Additional figures showing the FE-SEM and XRD of P-GO@Fe$_2$O$_3$/CNT/AC nanofibers, FE-SEM and XRD of F-CNF, survey spectrum of P-rGO@Fe$_x$S$_y$/N-CNT nanofibers, cyclic voltammetry curves of F-CNF-coated separator, and capacity utilization *vs.* C rate graph of P-rGO@Fe$_x$S$_y$/N-CNT nanofiber-coated separator. This information is available from the Wiley Online Library or from the author. *(Supplementary Materials)*

References

[1] S.-H. Chung and A. Manthiram, "Designing lithium–sulfur batteries with high-loading cathodes at a lean electrolyte condition," *ACS Applied Materials & Interfaces*, vol. 10, no. 50, pp. 43749–43759, 2018.

[2] R. Saroha, Y. H. Seon, B. Jin et al., "Self-supported hierarchically porous 3D carbon nanofiber network comprising Ni/Co/NiCo$_2$O$_4$ nanocrystals and hollow N-doped C nanocages as sulfur host for highly reversible Li-S batteries," *Chemical Engineering Journal*, vol. 446, no. 2, article 137141, 2022.

[3] S. Li, B. Jin, X. Zhai, H. Li, and Q. Jiang, "Review of carbon materials for lithium–sulfur batteries," *ChemistrySelect*, vol. 3, no. 8, pp. 2245–2260, 2018.

[4] W. Li, J. Hicks-Garner, J. Wang et al., "V$_2$O$_5$ polysulfide anion barrier for long-lived Li–S batteries," *Chemistry of Materials*, vol. 26, no. 11, pp. 3403–3410, 2014.

[5] W. Ren, W. Ma, S. Zhang, and B. Tang, "Nitrogen-doped carbon fiber foam enabled sulfur vapor deposited cathode for high performance lithium sulfur batteries," *Chemical Engineering Journal*, vol. 341, pp. 441–449, 2018.

[6] P. H. Wadekar, A. Ghosh, R. V. Khose, D. A. Pethsangave, S. Mitra, and S. Some, "A novel chemical reduction/co-precipitation method to prepare sulfur functionalized reduced graphene oxide for lithium-sulfur batteries," *Electrochimica Acta*, vol. 344, p. 136147, 2020.

[7] J. Xu, W. Zhang, Y. Chen, H. Fan, D. Su, and G. Wang, "MOF-derived porous N–Co_3O_4@N–C nanododecahedra wrapped with reduced graphene oxide as a high capacity cathode for lithium–sulfur batteries," *Journal of Materials Chemistry A*, vol. 6, no. 6, pp. 2797–2807, 2018.

[8] M. Wang, L. Fan, X. Wu et al., "Metallic $NiSe_2$ nanoarrays towards ultralong life and fast Li_2S oxidation kinetics of Li–S batteries," *Journal of Materials Chemistry A*, vol. 7, no. 25, pp. 15302–15308, 2019.

[9] G. Liu, Q. Sun, Q. Li, J. Zhang, and J. Ming, "Electrolyte issues in lithium–sulfur batteries: development, prospect, and challenges," *Energy & Fuels*, vol. 35, no. 13, pp. 10405–10427, 2021.

[10] G. He, S. Evers, X. Liang, M. Cuisinier, A. Garsuch, and L. F. Nazar, "Tailoring porosity in carbon nanospheres for lithium–sulfur battery cathodes," *ACS Nano*, vol. 7, no. 12, pp. 10920–10930, 2013.

[11] L. Fan, M. Li, X. Li, W. Xiao, Z. Chen, and J. Lu, "Interlayer material selection for lithium-sulfur batteries," *Joule*, vol. 3, no. 2, pp. 361–386, 2019.

[12] Z. Ren, Z. Zhao, K. Zhang, X. Wang, and Y. Wang, "Electrochemical behavior promotion of polysulfides by cobalt selenide/carbon cloth interlayer in lithium–sulfur batteries," *ChemElectroChem*, vol. 8, no. 8, pp. 1531–1536, 2021.

[13] P. Chongngam and A. Tubtimtae, "Structural, optical, and electrochemical characteristics of undoped and In^{3+}-doped tin antimony sulfide thin films for device applications," *Journal of Materials Science: Materials in Electronics*, vol. 34, p. 71, 2023.

[14] J. S. Lee, R. Saroha, S. H. Oh et al., "Rational design of perforated bimetallic (Ni, Mo) sulfides/N-doped graphitic carbon composite microspheres as anode materials for superior Na-ion batteries," *Small Methods*, vol. 5, no. 9, article e2100195, 2021.

[15] A. Jin, M.-J. Kim, K.-S. Lee, S.-H. Yu, and Y.-E. Sung, "Spindle-like Fe_7S_8/N-doped carbon nanohybrids for high-performance sodium ion battery anodes," *Nano Research*, vol. 12, no. 3, pp. 695–700, 2019.

[16] Y. Xu, T. Feng, Z. Cui, P. Guo, W. Wang, and Z. Li, "Fe_7S_8/FeS_2/C as an efficient catalyst for electrocatalytic water splitting," *International Journal of Hydrogen Energy*, vol. 46, no. 79, pp. 39216–39225, 2021.

[17] Y. Gan, F. Xu, J. Luo et al., "One-pot biotemplate synthesis of FeS_2 decorated sulfur-doped carbon fiber as high capacity anode for lithium-ion batteries," *Electrochimica Acta*, vol. 209, pp. 201–209, 2016.

[18] L. Xia, Z. Yang, B. Tang, F. Li, J. Wei, and Z. Zhou, "Carbon nanofibers with embedded Sb2Se3Nanoparticles as highly reversible anodes for Na-ion batteries," *Small*, vol. 17, no. 4, article 2006016, 2021.

[19] Y.-C. Zhang, Y. You, S. Xin et al., "Rice husk-derived hierarchical silicon/nitrogen-doped carbon/carbon nanotube spheres as low-cost and high-capacity anodes for lithium-ion batteries," *Nano Energy*, vol. 25, pp. 120–127, 2016.

[20] C. S. Kim, J. S. Lee, R. Saroha et al., "Porous nitrogen-doped graphene nanofibers comprising metal organic framework-derived hollow and ultrafine layered double metal oxide nanocrystals as high-performance anodes for lithium-ion batteries," *Journal of Power Sources*, vol. 523, article 231030, 2022.

[21] H. Li, L. Sun, Y. Zhang, T. Tan, G. Wang, and Z. Bakenov, "Enhanced cycle performance of Li/S battery with the reduced graphene oxide/activated carbon functional interlayer," *Journal of Energy Chemistry*, vol. 26, no. 6, pp. 1276–1281, 2017.

[22] M. Manoj, C. M. Ashraf, M. Jasna et al., "Biomass-derived, activated carbon-sulfur composite cathode with a bifunctional interlayer of functionalized carbon nanotubes for lithium-sulfur cells," *Journal of Colloid and Interface Science*, vol. 535, pp. 287–299, 2019.

[23] J. H. Kim, J. Seo, J. Choi et al., "Synergistic ultrathin functional polymer-coated carbon nanotube interlayer for high performance lithium–sulfur batteries," *ACS Applied Materials & Interfaces*, vol. 8, no. 31, pp. 20092–20099, 2016.

[24] J. Deng, J. Guo, J. Li, M. Zeng, and Z. Yang, "Functional separator with VGCF/PPY coating for high cyclic stability lithium–sulfur battery," *Materials Letters*, vol. 234, pp. 35–37, 2019.

[25] D.-R. Deng, C.-D. Bai, F. Xue, J. Lei, M.-S. Zheng, and Q.-F. Dong, "Multifunctional ion-sieve constructed by 2D materials as an interlayer for Li–S batteries," *ACS Applied Materials & Interfaces*, vol. 11, no. 12, pp. 11474–11480, 2019.

[26] P. Zeng, L. Huang, Y. Han, X. Zhang, R. Zhang, and Y. Chen, "Reduced shuttle effect of lithium–sulfur batteries by using a simple graphite-modified separator with a preformed SEI film," *ChemElectroChem*, vol. 5, no. 2, pp. 375–382, 2018.

[27] S. Jiang, M. Chen, X. Wang et al., "Honeycomb-like nitrogen and sulfur dual-doped hierarchical porous biomass carbon bifunctional interlayer for advanced lithium-sulfur batteries," *Chemical Engineering Journal*, vol. 355, pp. 478–486, 2019.

[28] J. Wei, H. Su, C. Qin, B. Chen, H. Zhang, and J. Wang, "Multifunctional Co_9S_8 nanotubes for high-performance lithium-sulfur batteries," *Journal of Electroanalytical Chemistry*, vol. 837, pp. 184–190, 2019.